Focusing of X-ray free-electron laser pulses using multilayer Laue lenses

MARGARITA ZAKHAROVA,[1] JIA CHYI WONG,[2] J. LUKAS DRESSELHAUS,[2] MAURO PRASCIOLU,[1] HOLGER FLECKENSTEIN,[1] CHUFENG LI,[1] IVAN DE GENNARO AQUINO,[1] DMITRY EGOROV,[1] WENHUI ZHANG,[1] ANDREW J. MORGAN,[3] KARTIK AYYER,[2,4] MARCIN SIKORSKI,[5] ROMAIN LETRUN,[5] RAPHAEL DE WIJN,[5] KONSTANTIN KHARITONOV,[5] DIOGO MELO,[5] ADAM ROUND,[5] RICHARD J. BEAN,[5] HENRY N. CHAPMAN,[1,2,6] AND SAŠA BAJT[1,2,*]

[1]*Center for Free-Electron Laser Science CFEL, Deutsches Elektronen-Synchrotron DESY, Notkestr. 85, 22607 Hamburg, Germany*

[2]*The Hamburg Centre for Ultrafast Imaging, Luruper Chaussee 149, 22761 Hamburg, Germany*

[3]*Department of Physics, University of Melbourne, VIC 3010, Australia*

[4]*Max Planck Institute for the Structure and Dynamics of Matter, 22761 Hamburg, Germany*

[5]*European XFEL GmbH, 22869 Schenefeld, Germany*

[6]*Department of Physics, University of Hamburg, Luruper Chaussee 149, 22761 Hamburg, Germany*

[*]*sasa.bajt@desy.de*

Abstract: Achieving the highest possible intensities of pulses at X-ray free-electron laser (XFEL) facilities entails focusing the X-ray beam to the smallest possible dimensions. Multilayer Laue lenses are volume diffractive optics that hold promise to achieve high intensities due to their high numerical aperture at hard X-ray wavelengths. These lenses are made by layer deposition and hence have a small aperture that is usually less than $100\,\mu m$. Consequently, they must withstand high intensities and heat loads if used to focus pulses of high energies. Here, we demonstrate the focusing of XFEL pulses using lenses made from layers of Mo_2C and SiC, which were chosen for their high efficiency and low beam heating. We show that lens alignment and characterisation can be carried out using attenuated XFEL pulses using the method of ptychographic X-ray speckle tracking, which also provides an approach for high-resolution projection imaging with XFEL pulses. The approach also gives quantitative information about the distribution of intensity in the focal plane, which is analysed here using plots of the encircled energy describing the proportion of the beam energy concentrated into a certain diameter, showing the possibility to reach $1.8 \times 10^{20}\,W\,cm^{-2}$ at a photon energy of 16.9 keV. No measurable change in the wavefront aberrations of the lenses could be detected after their use in an experiment for many days with unattenuated XFEL pulses, showing that the materials and mounting scheme presented here make these lenses suitable for sustained use at XFEL facilities.

1. Introduction

X-ray Free-Electron Lasers (XFELs) create extremely bright hard X-ray pulses with durations ranging from tens of femtoseconds down to below 1 fs. The beams possess almost complete transverse coherence, meaning that nearly the entire output of the source could be collected by an aberration-free imaging system and brought to a diffraction-limited focus with a width of about $\lambda/(2\,NA)$ for a numerical aperture NA and wavelength λ. In such a manner, extreme intensities

exceeding about 10^{19} W cm^{-2} can be reached that are high enough to induce non-linear processes in matter such as amplified spontaneous emission [1], two-photon absorption [2], and wave mixing [3]. Tight focusing may also increase the achievable resolution in single particle imaging experiments with XFEL pulses [4] and provide a strongly diverging beam for high-magnification flash projection imaging [5,6] or convergent-beam serial crystallography [7]. Kirkpatrick-Baez mirrors and beryllium compound refractive lenses are routinely used at beamlines at XFEL facilities to create focused probes that in some cases are as small as 250 nm width. These nanofocusing beamlines typically achieve peak intensities above 10^{19} W cm^{-2}. The highest X-ray intensities, exceeding 10^{22} W cm^{-2}, have been achieved using an advanced Kirkpatrick-Baez (AKB) imaging system based on Wolter type III mirrors [8]. This system focused an XFEL beam to a 7 nm spot at a wavelength of 1.36 Å (9.1 keV) and NA = 0.01. Tight focusing can also be used with XFEL pulses to form femtosecond-duration images at high spatial resolutions, by the method of magnified projection imaging, such as to image laser-induced transient densities of solids [9] and liquids [10]. Using synchrotron radiation, we recently obtained the smallest reported point spread function for an X-ray imaging system of 3 nm with a pair of multilayer Laue lenses (MLLs) that were aberration corrected using a refractive phase plate [11]. Following initial tests of MLLs at the European XFEL [12], here we detail an investigation of using MLLs to create tightly focussed beams at the European XFEL, and describe a simple wavefront sensing methodology that was used to characterise the focused beam. We find that MLLs can be used over the course of a week-long experiment period to focus unattenuated XFEL pulses, and that aberration correction is required to reach highest achievable intensities.

X-ray optical elements must withstand the high powers of XFEL pulses. This is most readily managed by grazing-incidence KB mirrors that spread absorbed energy over a large surface layer. The apertures of zone plates are typically smaller than 1 mm^2, and the largest MLLs fabricated to date are only about 100 μm tall. To utilize the high fluence, these optics therefore must operate under harsh conditions of high heat loads that can damage the elements or change their focusing properties [12,13]. In Sec. 2, we describe measures taken to create robust MLLs from layers of Mo$_2$C and SiC.

Accurate characterisation and alignment of focusing optics are needed to achieve highest intensities. The high intensities and shot to shot fluctuations of XFEL pulses make such characterisation challenging. An overview of several wavefront sensing approaches for lens alignment at XFEL beamlines [14] found that grating interferometry and speckle tracking methods are advantageous because test structures are placed out of focus and thus avoid beam damage. Those approaches require measurements at two detector distances, which becomes incompatible when applied to lenses of high NA as used here. Ptychographic X-ray Speckle Tracking (PXST) is a non-interferometric wavefront sensing and imaging technique developed specifically for characterizing highly divergent wavefields such as those produced by high-NA MLLs [15,16]. It is further attractive for XFEL applications since it utilises the same pixel-array detector as used for diffraction measurements. In Secs. 3 and 4 we find that it works well with XFEL pulses. As described in Sec. 5, the lenses show promise to create intense focused pulses and highly diverging beams for high-magnification projection imaging directly on a JUNGFRAU detector [17].

2. Multilayer Laue lens fabrication and characterization

Multilayer Laue lenses are volume-diffractive optics that offer very high NA and diffraction efficiency [18,19]. To achieve high NA, the MLL has to be wedged so that Bragg diffraction by the layers can occur across the entire lens aperture for a particular fixed wavelength. The properties of MLLs such as efficiency, bandwidth acceptance, and wavelength range have been discussed elsewhere [20–22].

A pair of wedged off-axis MLLs were constructed from a Mo_2C/SiC multilayer structure consisting of 18 975 bilayers. The multilayer was made by magnetron sputtering onto a flat substrate that was shadowed by a pair of straight-edged masks to provide the required tilt profiles for the lenses [19,23]. When Mo_2C/SiC multilayers are heated in an oven at temperatures up to 300°C, we found that their periods remain unchanged but their stress changes with temperature [24]. We further observed that initial annealing relaxes the stress which then remains stable through subsequent heating cycles. Numerical simulations [22] predict that when exposed to 1 mJ XFEL pulses at pulse rates less than about 10 kHz, the temperature in Mo_2C/SiC MLLs will not exceed 280°C, so we annealed the deposited structure at 250°C for 1 h to ensure it would be unaffected by XFEL-induced heating. After annealing the structure, two lenses were sliced and pre-thinned using a Xe-plasma focused ion beam (PFIB, Thermo Fisher Scientific Inc., USA). One lens had a total height of 88 μm and a focal length of 4 mm at a photon energy of 16.9 keV. The maximum period of the layers in this lens was 12 nm, giving an offset of the lens aperture from the optical axis of 28 μm. The minimum period was 2 nm, yielding a full convergence angle of 18 mrad (NA = 0.009). The second lens had a height of 80 μm and a focal length of 4 mm.

Our choice of materials (Mo_2C and SiC) was a compromise between achieving high diffraction efficiency [24] and low absorbance and hence reduced beam heating. Each lens was mounted on a 7 mm × 5 mm double-side polished 100 μm thick chemical vapor deposition (CVD) diamond wafer as depicted in Fig. 1. Diamond has high thermal conductivity, excellent thermal stability, and low X-ray absorption. The diamond plate was attached to the edge of an aluminum holder using glue. The lens was positioned over a 110 μm × 110 μm square slot milled into the top edge of the diamond. A custom-developed thermal glue was applied between the MLL and the diamond via a glass micropipette positioned with a Kleindiek micromanipulator (Kleindiek Nanotechnik GmbH, Germany) to create a thermal contact. The 30 μm diameter glass micropipette was prepared from a borosilicate glass capillary pulled using a laser-based micropipette puller (P-2000, Sutter Instrument, USA). The glue consisted of a blend of epoxy and carbon glue, mixed with propylene glycol monomethyl ether acetate (PGMEA) and a hardener. The final proportions of each component were determined experimentally to achieve the optimal viscosity for the glue, allowing it to be applied with the micropipette. The entire piece was left at room temperature for 16 hours, after which it was heated for 3.5 hours on a hot plate at 130°C. Once cooled to room temperature, the lens was thinned to 19 μm using the PFIB. This is the thickness in the beam propagation direction that gives maximum diffraction efficiency for this material pair at 16.9 keV photon energy [24]. This efficiency was measured in our laboratory X-ray setup (described in [25]) to be about 75 %, resulting in a combined efficiency of the two lenses of 56 %.
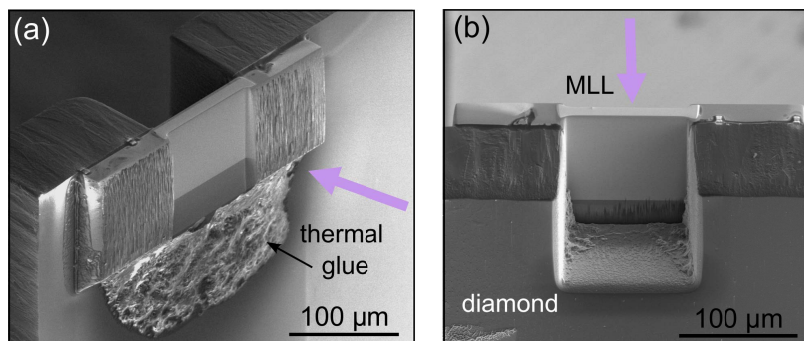
Fig. 1. SEM images of multilayer Laue lenses mounted on a diamond plate with thermal glue: (a) upstream view, (b) downstream view. The purple arrow indicates the direction of X-rays.

The high convergence angles of beams focused by MLLs demand a specialized method of wavefront sensing for alignment and characterization. We have developed the method of ptychographic X-ray speckle tracking (PXST) to meet this need [15,16,26]. Magnified projection holograms of a test object are recorded directly on the JUNGFRAU detector. As in non-interferometric methods such as Hartmann sensing, any phase gradient of the wavefield causes a local tilt in ray propagation, which leads to a local distortion of the hologram. The actual structure of the test object is not known *a priori* so these distortions are made apparent by stepping the object transversely across the beam. An iterative approach is used to solve for the distortion field (proportional to the phase gradient of the wavefront) and the undistorted projection hologram of the object, taking into account local wavefront curvature. Using our *pyrost* software for wavefront determination, integration of the phase gradients is performed via a cosine transform integration [26]. The approach alleviates the need for a separate reference image measurement. PXST offers high angular sensitivity and imaging resolution and is robust against errors in the registered sample positions and intensity scaling, making it resilient to beam-pointing fluctuations experienced at XFELs.

Since PXST does not require high coherence, we also use the method to separately characterize the wavefront of each single lens (focusing only in one direction) with a laboratory source [25] prior to their use at the European XFEL. Measurements were also carried out at the P11 beamline of the PETRA III synchrotron radiation facility after the XFEL experiments to check for any changes in the performance of the lenses, using instrumentation and procedures largely similar to those used at the European XFEL as described below in Sec. 3. At P11, an EIGER 16M detector (Dectris, Switzerland) was used at a distance of 3.42 m downstream of the lenses, instead of a JUNGFRAU detector [27] at the European XFEL placed 1.47 m from the lens focus. The holograms of a Siemens star object were recorded at magnifications of about 1600, 3000 (European XFEL) and 9000 (P11) as the object was stepped across the field of view as defined by the diverging beam. The high magnification together with direct photon detection provided a high sensitivity for the wavefront measurements [15].

3. Projection imaging and wavefront sensing with XFEL pulses

The experiment was conducted at the SPB/SFX instrument [28] of the European XFEL facility on the downstream optical table of the experimental hutch in ambient air. Single pulses at a repetition rate of 10 Hz and 16.9 keV photon energy were pre-focused using beryllium compound refractive lenses (CRLs) located 4 m upstream of the MLLs. These produced a beam of approximately 200 μm width at the plane of the MLLs. This was shaped with a pair of tungsten slits to slightly overfill the 80 μm × 88 μm aperture of the MLLs. Based on the lens efficiency and the total counts in the beam diverging from focus, the pulse energy incident on the lenses was estimated at 500 mJ out of a pulse energy of 1.4 mJ measured by the upstream gas monitor detector.

The MLLs were positioned using separate hexapods (SmarAct GmbH, Germany), one mounted upside down and above the other. Using an optical microscope (Keyence International NV/SA, Belgium), the separation of the lenses was initially set to 0.8 mm, the difference of their nominal focal lengths (see Fig. 2(a)). The lenses were brought into their Bragg condition and overlapped with each other by observing the extinction of their transmitted beams on a diagnostic scintillating screen [28] positioned 4 m downstream. This procedure was performed using an attenuated XFEL beam (transmission 0.003%).

For the fine alignment and characterisation of the lenses, the beam was measured directly on the JUNGFRAU detector positioned 1.47 m downstream from the MLL focus, with an attenuated incident beam (0.86% transmission). At this distance, the beam diverging from the focus measured 26 mm × 26 mm. While the zero-order beam transmitted by the lenses passes safely through a hole in the detector, the two one-dimensional foci (focused order of one lens combined with the zero order of the other) diverge to two lines of 26 mm length and about 90 μm
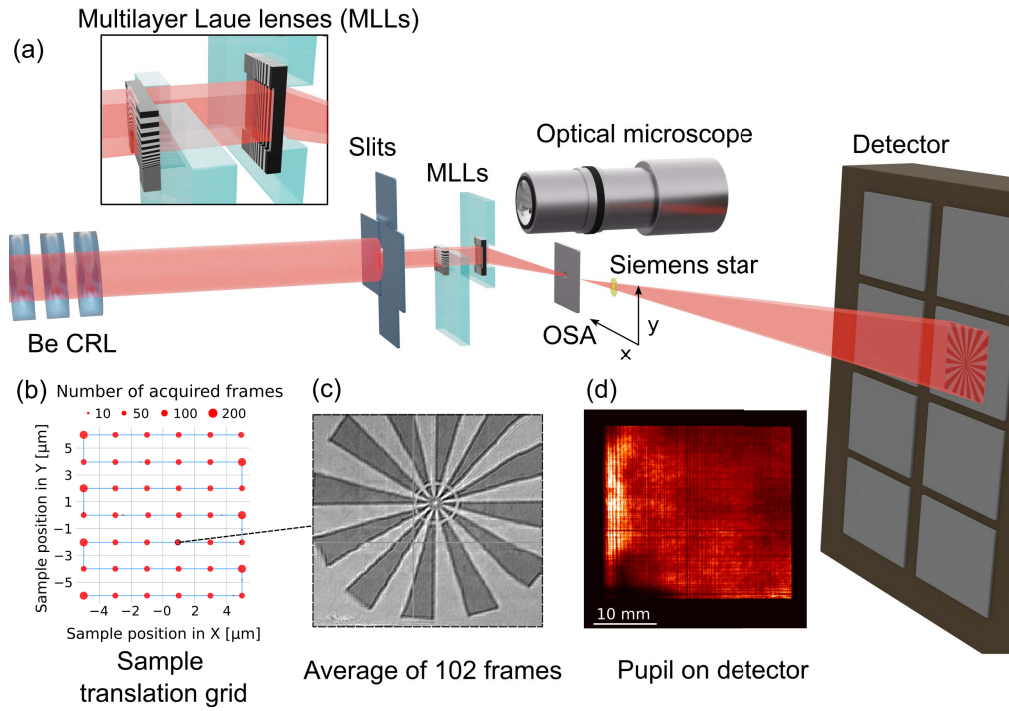
Fig. 2. (a) Experimental setup at the SPB/SFX beamline consisting of prefocusing optics (beryllium compound refractive lenses - Be CRLs), beam shaping slits, two crossed MLLs, order-sorting aperture (OSA) and an object (Siemens star). The object was scanned on a two-dimensional 6×7 grid shown in (b). The step size for the grid was $2\,\mu m$ for the scan with magnification 1600 (e.g. averaged frame shown in Fig. 2(c)) and $1\,\mu m$ for the scan with magnification 3000 (Fig. 4(a-e)). The magnified holograms of the Siemens star were recorded by the JUNGFRAU detector. (c) An average of 102 frames that were acquired per position, normalized by the flat field. (d) Pupil of the crossed MLL pair on the detector without the object.
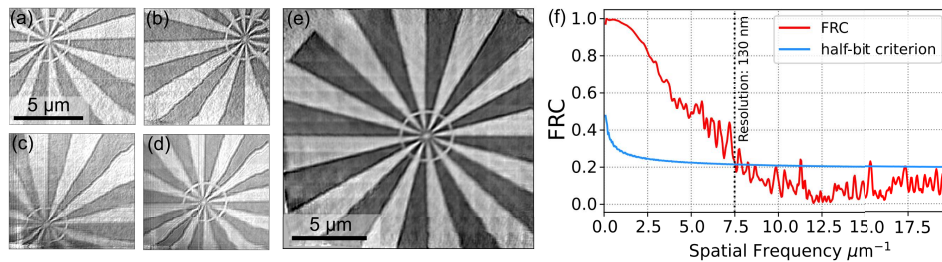
Fig. 3. Results of the PXST reconstruction: (a-d) Siemens star holograms (average of 98 frames) recorded at different positions on the sample translation grid. Distortions of the Siemens star reflect the presence of wavefront aberrations. (e) Reconstructed undistorted reference hologram of the Siemens star object obtained using PXST. (f) Fourier ring correlation (FRC) of the reference hologram, using the half-bit threshold, reveals a spatial resolution of 130 nm.

width. These could be blocked by an L-shaped beam stop placed near the detector, but for initial alignment the lenses were rotated about the beam axis to orient them orthogonal to each other
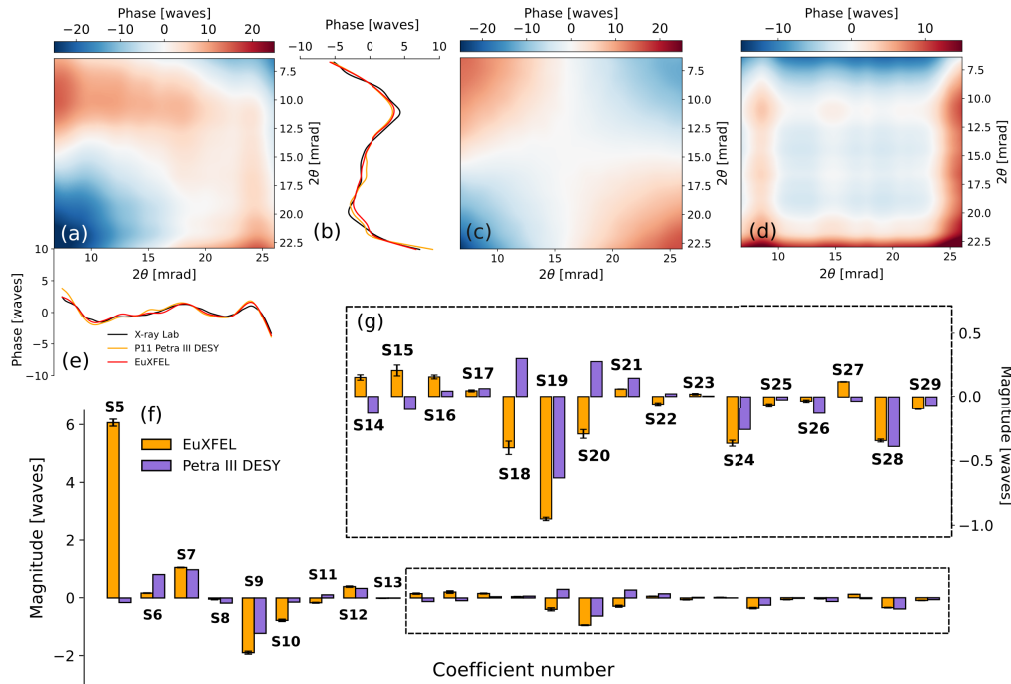
Fig. 4. Results of the PXST wavefront reconstruction: The two-dimensional phase map (a) was decomposed into two orthogonal components, corresponding to the vertically (b) and horizontally (e) focusing MLLs. The black lines in (b, e) represent the wavefronts measured for each lens separately using a laboratory X-ray source prior to the European XFEL experiment, while orange lines indicate the two orthogonal components retrieved from the measurement at the synchrotron after the week-long XFEL experiment. (c) The difference between the measured wavefront and a wavefront constructed from the two 1D components with perfect orthogonality between them, revealing strong oblique astigmatism. (d) The two-dimensional wavefront of the same lens pair, as measured at P11 beamline of PETRA III. (f) Coefficients of a Zernike-like decomposition of the phase maps. Orange indicates measurements at European XFEL and purple at PETRA III (after the XFEL experiment). The inset (g) shows the S_{14} to S_{29} coefficients on an expanded scale.

(and to the detector pixels). A square order-sorting aperture (OSA) of $30\,\mu m$ width was placed just upstream of the common focus of the lenses to block scattering from the lenses as well as to attenuate the zero-order components of the MLLs.

PXST measurements for evaluation of the wavefront were made by recording holograms of the Siemens star object placed at a defocus of $500\,\mu m$ where the beam size is about $10\,\mu m$. The magnification of the holograms was therefore 2940 so that each $75\,\mu m$ wide pixel of the JUNGFRAU detector maps to an effective pixel size of $\delta = 25\,nm$. A dataset of overlapping magnified holograms was collected along with the registered sample positions (see Fig. 3(a-d)). Due to the extent and variability of the Siemens star test object features, only a small number of translation steps are needed to probe aberrations across the lens aperture which can be achieved in a few minutes. A typical scan with 6×7 positions with $1\,\mu m$ step size is plotted in Fig. 2(b). At each position, about 100 frames were recorded (ranging from 98 to 202 frames). The number of frames collected per position was not constant due to the sample positioning and the train-triggered data collection at the European XFEL. Frames acquired between grid positions were discarded. Our robust PXST method [26] was then used to recover both the undistorted

projection hologram, called the reference image, and the wavefront map. The reference image is depicted in Fig. 3(e) and the wavefront map is shown in Fig. 4(a).

The Siemens star test sample had a diameter of 20 μm and consisted of 12 radial gold "spokes" with a smallest half pitch of 50 nm and a projected thickness ranging from 600 nm to 900 nm. Since this is thinner than $\delta/(2\text{NA}) = 1.4$ μm, variations in magnification through the thickness of the object can be neglected. With the beam transmission of 0.86%, the Siemens star remained undamaged throughout the scans at a defocus of 500 μm, but when this was reduced to 250 μm the gold structure of the Siemens star was damaged by the higher intensity of the smaller beam.

The spatial resolution of the reference image was evaluated by computing the Fourier ring correlation (FRC) [29], plotted in Fig. 3(f). For this, the dataset of 6×7 steps was split into two half datasets, each containing 49 frames at every position, from which two independent Siemens star projection holograms were obtained. These were smoothed using Gaussian and Hann window filters before calculating the FRC to reduce high-frequency noise and edge artifacts. A half-bit criterion for the FRC curve indicated a spatial resolution of the projection image of 130 nm. While the projection image is equivalent to a defocused image obtained with a full-field microscope, this should be a reasonable indicator of the resolution obtainable for an in-focus reconstruction such as by near-field ptychography [6].

After the MLL alignment and wavefront characterization, detailed in Sec. 4, the lenses were used to focus an unattenuated XFEL beam of 16.9 keV at 10 Hz during a week-long experimental campaign. Lens angles had to be occasionally adjusted due to small changes in beam pointing, minor drifts in hexapod positions, and variations in heat load resulting from beam interruptions.

4. Wavefront analysis and alignment

The PXST wavefront measurements were used to optimize the alignment of the lenses. The wavefront of each lens does not change significantly throughout the rocking curve of the lens, so no further lens tilt is required after achieving the highest throughput of each lens [30]. However, both lenses need to be positioned to create a common focus. Changing the longitudinal spacing between the two lenses separates the horizontal and vertical foci which results in a contribution to the wavefront of vertical astigmatism (or 0-90° astigmatism) proportional to $\theta_x^2 - \theta_y^2$ where θ_x, θ_y are the angular coordinates of the lens pupil. Rotating one lens about the optical axis relative to the other gives rise to the second orthogonal mode of astigmatism—oblique or 45° astigmatism proportional to $\theta_x\theta_y$. The dependency of the induced wavefront aberrations (in radians) on the lens displacement L and rotation angle α (relative to their optimal positions) can be evaluated as

$$\Phi_L(\theta_x, \theta_y) = \frac{\pi}{\lambda}\frac{L}{2}\left(\theta_x^2 - \theta_y^2\right) \tag{1}$$

$$\Phi_\alpha(\theta_x, \theta_y) = \frac{\pi}{\lambda}(2f\sin\alpha)\,\theta_x\theta_y \tag{2}$$

where f is the average focal length of the lenses, and the angular coordinates range from $-\text{NA}$ to $+\text{NA}$ for a square aperture. Here, the change in the wavefront was calculated by displacing or rotating each lens in opposite directions by either $L/2$ or $\alpha/2$ from their ideal positions. Fine alignment of the lenses is achieved by measuring the wavefront and adjusting L and α to reduce the two astigmatism terms.

The wavefront aberration obtained from the XFEL PXST measurements is shown in Fig. 4 after subtracting the piston, tilt and defocus terms. The wavefront is dominated by strong oblique astigmatism. The low-order aberration modes can be quantified by decomposing the wavefront into a sum of orthonormal Zernike-like polynomials. Zernike polynomials are defined on a circular aperture, and the set of polynomials used here were derived from those via a Gram-Schmidt orthogonalization over the rectangular aperture of the MLL pair [31,32]. The coefficients of this decomposition are plotted in Fig. 4(f) as the orange bars. The ordering of

the terms follows Noll's sequence of Zernike polynomials [33] where the magnitude of oblique astigmatism is S_5 and that of vertical astigmatism is S_6. The piston, tilt, and defocus terms (S_1 - S_4) are omitted from the plot. Besides the strong oblique astigmatism, other main contributions are vertical and horizontal coma (S_7 and S_8) and oblique secondary astigmatism (S_{13}). The root mean square (RMS) wavefront error computed from the sum of the squares of the Zernike coefficients is 49.8 ± 0.1 rad. The contribution of the oblique astigmatism was $S_5 = 38.1 \pm 0.1$ rad and if this term were eliminated the wavefront RMS would be 31.9 ± 0.1 rad.

From Eq. (2), and the expression of the orthonormal polynomial $Z_5(\theta_x, \theta_y) = (3/2)\theta_x \theta_y / \mathrm{NA}^2$, we find that the oblique astigmatism of $S_5 = 38.1 \pm 0.1$ rad would require a rotation of one lens by $\alpha = 0.22°$. This adjustment is slightly larger than the error to which the two lenses were initially placed by aligning the 1D line foci parallel to the rows and columns of the JUNGFRAU detector. Each line extended over 350 pixels on the detector and about a half-pixel displacement (or $0.08°$ rotation) could be detected. In addition, the wavefront of the beam focused by the CRLs could have been astigmatic. Due to limited time, the oblique astigmatism was not minimised at the European XFEL, but we can determine the potential performance by comparing with subsequent measurements made using synchrotron radiation.

When two 1D-focusing lenses are aligned orthogonally to create a 2D focus, not only are the astigmatism terms zero but the wavefront phase is completely separable into a sum of a function of only θ_x and a function of only θ_y. Indeed, these functions should match the 1D wavefronts of the individual lenses as measured at the laboratory source before the XFEL experiment, assuming no change to the structure of the lenses. The wavefront phase can be separated into functions of the horizontal and vertical directions by integrating the phase along the respective directions as plotted in Figs. 4(b) and (e). As seen in those two plots, there is close agreement between the 1D wavefronts extracted from the measurements made at the XFEL, at the P11 beamline, and as measured from the individual lenses using the laboratory source. The RMS wavefront error of each of the two individual lenses was 1.1 ± 0.3 waves and 2.3 ± 0.5 waves, and was 5.8 waves RMS for the 2D wavefront after alignment. The difference between the wavefront measured at the XFEL and that reconstituted from the separated horizontal and vertical terms displays the non-separable terms, shown in Fig. 4(c). This is dominated by oblique astigmatism, as expected from the plot of Zernike coefficients. (The first Zernike terms that are not separable are S_5, S_9, S_{10}, and S_{13}.) The wavefront obtained from the lenses at the P11 beamline, which was done after alignment of both astigmatism modes, is shown in Fig. 4(d) and its Zernike decomposition is shown in Fig. 4(f) as the purple bars.

5. Point spread function (PSF) and energy density

Since the XFEL beam has almost complete spatial coherence, the point spread function (PSF) well represents the actual intensity profile of the focused beam. The PSF of the lens pair as aligned at the European XFEL is shown in Fig. 5(a). It was obtained from the square modulus of the Fourier transform of the aperture function constructed from the retrieved wavefront phase (Fig. 4(a)) and amplitude (the square root of the pupil intensity of Fig. 2(d)). The strong oblique astigmatism is evident in Fig. 5(a) by the diagonal elongation of the PSF. The full-width at half-maximum (FWHM) of the focus along the horizontal and vertical directions is $5\,\mathrm{nm} \times 6\,\mathrm{nm}$, while the FWHM along the diagonal is 14 nm x 4 nm as depicted in Fig. 5(c) for the diagonal indicating larger FWHM. The PSF of the lens pair with compensated astigmatism as measured at the P11 beamline is shown in Fig. 5(b). The FWHM of the PSF is 4.8 nm along the horizontal direction and 5.3 nm in the vertical, both improved as compared with the as-aligned configuration. The FWHM along the diagonal is significantly reduced as plotted in Fig. 5(d).

The peak intensity in the focal spot was calculated by measuring the total pulse energy in the beam diverging from the 2D focus by summing detector counts while attenuating the beam incident on the lenses. Accounting for that attenuation and an assumed detector efficiency of
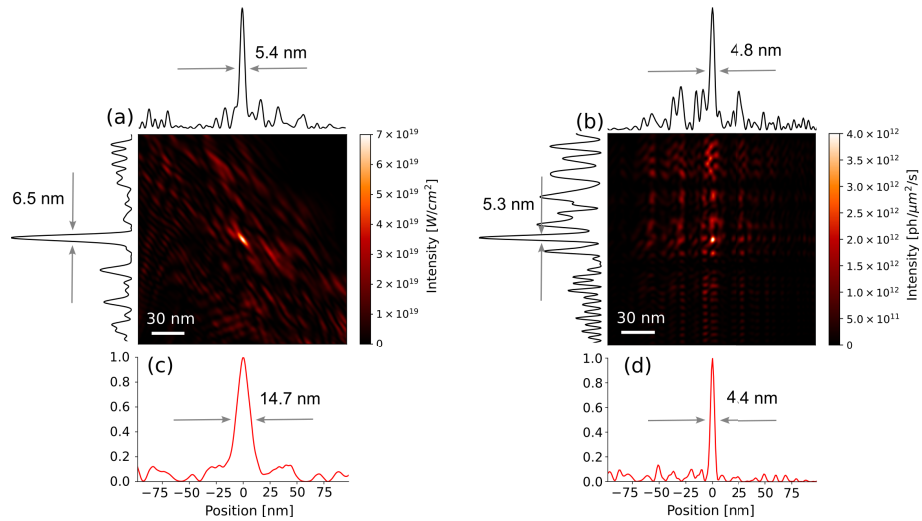
Fig. 5. (a) Point spread function (PSF) of the lens pair obtained from the measured wavefront at XFEL. (b) PSF obtained from measurements at the synchrotron. For both PSFs the horizontal and vertical profiles are shown along the respective axes. (c,d) The corresponding diagonal 1D profiles for PSFs shown in (a) and (b), respectively. The diagonal 1D profile is from the upper left to the lower right corner of the PSF image.

40 % (as determined from the sensor thickness), the pulse energy in the focused beam was found to be 270 ± 50 mJ. Given a pulse length of 50 fs, we estimate the intensity of 1×10^{19} W cm^{-2} within the FWHM of the focus (along the diagonal it is considered here to be 14.7 nm × 4.1 nm), with peak intensity of about 7×10^{19} W cm^{-2}. If the lens alignment had matched the precision achieved at the P11 beamline – effectively eliminating astigmatism – an intensity of around 6×10^{19} W cm^{-2} could have been reached within a tighter FWHM focus of 5 nm × 4 nm, with a corresponding peak intensity of 1.8×10^{20} W cm^{-2}. For comparison, the diffraction-limited performance of the MLLs under the same conditions would yield an intensity of 4×10^{21} W cm^{-2} within a 3 nm × 3 nm focus, with peak intensity of 2×10^{22} W cm^{-2}.

As is clear from Fig. 5, wavefront aberrations direct energy out of the focal spot. We calculated the encircled energy of the PSF to characterise the distribution of energy in the focal plane. This quantity gives the ratio of the energy within a circle centered on the PSF centroid to the total energy in that plane, as a function of the radius of the circle. Encircled energy plots are shown in Fig. 6(a) for the as-aligned lenses used at the European XFEL as well as for the lenses aligned to compensate astigmatism. One can see that the 45° astigmatism significantly impacted the energy density in the focus, with 20 % of the energy spread over a circle with a radius of 100 nm. We estimate the intensity encircled in this radius to be 4.2×10^{18} W cm^{-2}. In the absence of these astigmatic aberrations, 20 % of the energy would be concentrated into a 45 nm radius, resulting in an estimated intensity of 1.2×10^{19} W cm^{-2}.

The intensity distribution around the focal spot was also evaluated through focus by numerically propagating the wavefront by adding a quadratic defocus term to the wavefront phase. The encircled energy was then computed as a function of radius and defocus as shown in Figs. 6 for the as-aligned case (b) and the astigmatism-corrected case measured at the synchrotron (c). Such maps are useful in indicating the effective depth of focus of the optical system, which is significantly larger than for a diffraction-limited lens.
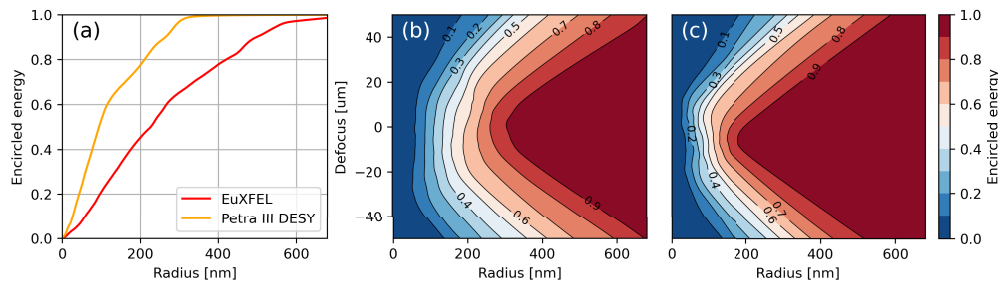
Fig. 6. (a) Encircled energy curves showing the fraction of energy in the focal region as a function of radius. (b, c) Encircled energy distribution for varying defocus distances, illustrating the depth of focus: (b) for the wavefront measured at European XFEL, (c) for the wavefront measured at P11 beamline of the PETRA III synchrotron. All measurements were conducted using the same lens pair.

6. Conclusions

This study demonstrates that Mo_2C/SiC multilayer Laue lenses (MLLs) can tightly focus XFEL beams, and that ptychographic X-ray speckle tracking (PXST) can be used at these sources to characterize the wavefront and align the lenses. Thermal annealing, and robust mounting and gluing to a diamond substrate ensured the mechanical and thermal stability of the MLLs under sustained XFEL operating conditions of unattenuated pulses at a 10 Hz pulse rate over a week-long experiment. Indeed, wavefront characterisation of the lenses before and after their use at the European XFEL showed no detectable change in their performance.

The PXST method was found to be well suited both for projection imaging and wavefront sensing with XFEL pulses. Measurements are carried out using the same pixel-array detector in place for diffraction experiments—here, a JUNGFRAU detector. Projection holograms of a structured object were recorded at a magnification of almost 3000, giving an effective pixel size of the holograms of 25 nm. While the holograms are distorted due to wavefront aberrations, these are corrected in the PXST analysis. The resolution of these was estimated to be 130 nm. This is larger than the effective pixel size, perhaps due to beam pointing fluctuations or sample stage motion while averaging each hologram over many attenuated pulses in order not to damage the object. The PXST wavefront map can also be used to correct distortions in single-shot holograms recorded at high intensities.

The wavefront map obtained by PXST provides quantitative information about the focus, as is required for many experiments using tightly focused beams. While it is possible to achieve a point spread function with a focus spot width smaller than 10 nm, wavefront aberrations dictate that only a small fraction of the total energy of the beam enters that spot. An analysis of the encircled energy showed that it should be possible to concentrate 20 % of the total focused beam energy into a circle of 45 nm radius, corresponding to an intensity of $1.2 \times 10^{19} \, \text{W cm}^{-2}$. This can be compared with the performance of diffraction-limited lenses which would give $2 \times 10^{22} \, \text{W cm}^{-2}$.

Future experiments at XFELs can take advantage of MLLs for high-resolution projection imaging or for producing the highest possible pulse intensities. Single-pulse projection imaging could be carried out at resolutions of tens of nanometers as determined by the detector pixel size and the imaging magnification, for damage-free imaging of biological objects such as cells or time-resolved imaging of dynamic processes. In this case, the wavefront determined by PXST would be used to correct each hologram. Further studies are required to determine what pulse energies can be used for imaging high-speed processes at megahertz rates [5]. When using pulse energies of 1 mJ or more and if the hologram is spread over 1000×1000 pixels of the detector, each pixel may receive over 10^5 photons under conditions tested here (with a shot noise of 0.3%).

This exceeds the capacity of pixel array detectors and so a different detector technology may be required to record such bright-field low-noise images.

Future efforts in focusing XFEL pulses with MLLs will use PXST wavefront measurements to characterize and improve upstream optics in the beamline, including the use of refractive phase plates to compensate aberrations [11,34] or to create tailored focus profiles for diffraction or imaging experiments. Upstream optics could also be improved to couple more of the incident beam onto the MLLs. In this way it seems feasible to reach intensities above $10^{21}\,\mathrm{W\,cm^{-2}}$ to offer extreme intensities for applications such as single-particle imaging, convergent-beam crystallography, non-linear spectroscopy, and the investigation of matter under extreme conditions.

Disclosures. The authors declare no conflicts of interest.

Data availability. Data underlying the results presented in this paper are not publicly available at this time but may be obtained from the authors upon reasonable request.

References

1. H. Yoneda, Y. Inubushi, K. Nagamine, *et al.*, "Atomic inner-shell laser at 1.5-ångström wavelength pumped by an x-ray free-electron laser," Nature **524**(7566), 446–449 (2015).
2. M. Fuchs, M. Trigo, J. Chen, *et al.*, "Anomalous nonlinear x-ray compton scattering," Nat. Phys. **11**(11), 964–970 (2015).
3. T. E. Glover, D. M. Fritz, M. Cammarata, *et al.*, "X-ray and optical wave mixing," Nature **488**(7413), 603–608 (2012).
4. T. Ekeberg, D. Assalauova, J. Bielecki, *et al.*, "Observation of a single protein by ultrafast x-ray diffraction," Light: Sci. Appl. **13**(1), 15 (2024).
5. P. Vagovič, T. Sato, L. Mikeš, *et al.*, "Megahertz x-ray microscopy at x-ray free-electron laser and synchrotron sources," Optica **6**(9), 1106–1109 (2019).
6. W. Zhang, J. L. Dresselhaus, H. Fleckenstein, *et al.*, "Fast and efficient hard X-ray projection imaging below 10 nm resolution," Opt. Express **32**(17), 30879–30897 (2024).
7. H. N. Chapman, C. Li, S. Bajt, *et al.*, "Convergent-beam attosecond x-ray crystallography," Struct. Dyn. **12**(1), 014301 (2025).
8. J. Yamada, S. Matsuyama, I. Inoue, *et al.*, "Extreme focusing of hard X-ray free-electron laser pulses enables 7 nm focus width and $10^{22}\,\mathrm{W\,cm^{-2}}$ intensity," Nat. Photonics **18**(7), 685–690 (2024).
9. A. Schropp, R. Hoppe, V. Meier, *et al.*, "Imaging shock waves in diamond with both high temporal and spatial resolution at an XFEL," Sci. Rep. **5**(1), 11089 (2015).
10. M. Vassholz, H. P. Hoeppe, J. Hagemann, *et al.*, "Pump-probe x-ray holographic imaging of laser-induced cavitation bubbles with femtosecond FEL pulses," Nat. Commun. **12**(1), 3468 (2021).
11. J. L. Dresselhaus, M. Zakharova, N. Ivanov, *et al.*, "X-ray focusing below 3 nm with aberration-corrected multilayer Laue lenses," Opt. Express **32**(9), 16004–16015 (2024).
12. M. Prasciolu, K. T. Murray, N. Ivanov, *et al.*, "On the use of multilayer Laue lenses with X-ray free electron lasers," in *International Conference on X-Ray Lasers 2020*, vol. 11886 (SPIE, 2021), pp. 159–166.
13. C. David, B. Nöhammer, H. H. Solak, *et al.*, "Differential x-ray phase contrast imaging using a shearing interferometer," Appl. Phys. Lett. **81**(17), 3287–3289 (2002).
14. M. Seaberg, R. Cojocaru, S. Berujon, *et al.*, "Wavefront sensing at x-ray free-electron lasers," J. Synchrotron Radiat. **26**(4), 1115–1126 (2019).
15. A. J. Morgan, K. T. Murray, M. Prasciolu, *et al.*, "Ptychographic X-ray speckle tracking with multi-layer Laue lens systems," J. Appl. Crystallogr. **53**(4), 927–936 (2020).
16. A. J. Morgan, K. T. Murray, H. M. Quiney, *et al.*, "*speckle-tracking*: a software suite for ptychographic X-ray speckle tracking," J. Appl. Crystallogr. **53**(6), 1603–1612 (2020).
17. F. Leonarski, S. Redford, A. Mozzanica, *et al.*, "Fast and accurate data collection for macromolecular crystallography using the JUNGFRAU detector," Nat. Methods **15**(10), 799–804 (2018).
18. H. Yan, H. C. Kang, R. Conley, *et al.*, "Multilayer Laue lens: A path toward one nanometer x-ray focusing," X-Ray Opt. Instrum. **2010**, 1–10 (2010).

19. S. Bajt, M. Prasciolu, H. Fleckenstein, *et al.*, "X-ray focusing with efficient high-NA multilayer Laue lenses," Light: Sci. Appl. **7**(3), 17162 (2018).

20. H. Yan, J. Maser, A. Macrander, *et al.*, "Takagi-Taupin description of x-ray dynamical diffraction from diffractive optics with large numerical aperture," Phys. Rev. B **76**(11), 115438 (2007).

21. H. Yan, R. Conley, N. Bouet, *et al.*, "Hard x-ray nanofocusing by multilayer Laue lenses," J. Phys. D: Appl. Phys. **47**(26), 263001 (2014).

22. Z. Rek, H. N. Chapman, B. Šarler, *et al.*, "Numerical simulation of heat load for multilayer Laue lens under exposure to XFEL pulse trains," Photonics **9**(5), 362 (2022).

23. M. Prasciolu, A. Leontowich, J. Krzywinski, *et al.*, "Fabrication of wedged multilayer Laue lenses," Opt. Mater. Express **5**(4), 748–755 (2015).

24. M. Zakharova, Z. Rek, B. Šarler, *et al.*, "On the thermal stability of multilayer optics for use with high x-ray intensities," Opt. Mater. Express **14**(8), 1933–1948 (2024).

25. J. L. Dresselhaus, H. Fleckenstein, M. Domaracký, *et al.*, "Precise wavefront characterization of x-ray optical elements using a laboratory source," Rev. Sci. Instrum. **93**(7), 073704 (2022).

26. N. Ivanov, J. L. Dresselhaus, J. Carnis, *et al.*, "Robust ptychographic X-ray speckle tracking with multilayer Laue lenses," Opt. Express **30**(14), 25450 (2022).

27. A. Mozzanica, A. Bergamaschi, S. Cartier, *et al.*, "Prototype characterization of the JUNGFRAU pixel detector for SwissFEL," J. Instrum. **9**(05), C05010 (2014).

28. A. P. Mancuso, A. Aquila, L. Batchelor, *et al.*, "The Single Particles, Clusters and Biomolecules and Serial Femtosecond Crystallography instrument of the European XFEL: initial installation," J. Synchrotron Radiat. **26**(3), 660–676 (2019).

29. M. van Heel and M. Schatz, "Fourier shell correlation threshold criteria," J. Struct. Biol. **151**(3), 250–262 (2005).

30. H. N. Chapman and S. Bajt, "A ray-trace analysis of x-ray multilayer Laue lenses for nanometer focusing," J. Opt. **22**(11), 115610 (2020).

31. W. Swantner and W. W. Chow, "Gram–Schmidt orthonormalization of Zernike polynomials for general aperture shapes," Appl. Opt. **33**(10), 1832–1837 (1994).

32. V. N. Mahajan and G. Ming Dai, "Orthonormal polynomials in wavefront analysis: analytical solution," J. Opt. Soc. Am. A **24**(9), 2994–3016 (2007).

33. R. J. Noll, "Zernike polynomials and atmospheric turbulence," J. Opt. Soc. Am. **66**(3), 207–211 (1976).

34. F. Seiboth, A. Schropp, M. Scholz, *et al.*, "Perfect x-ray focusing via fitting corrective glasses to aberrated optics," Nat. Commun. **8**(1), 14623 (2017).